

CHANDRA OBSERVATIONS OF CIRCUMNUCLEAR STAR FORMATION IN NGC 3351

DOUGLAS A. SWARTZ,¹ MIHOKO YUKITA,² ALLYN F. TENNANT,³ ROBERTO SORIA,⁴ AND KAJAL K. GHOSH¹

Received 2005 December 30; accepted 2006 March 24

ABSTRACT

The nearby SB(r)b galaxy NGC 3351 (M95) displays an ~ 600 pc diameter star-forming circumnuclear ring fueled by gas accreted through a stellar bar. The X-ray emission from this region is composed of numerous pointlike sources embedded in hot ($kT = 0.5 \pm 0.1$ keV), nonuniform diffuse gas. Most of the pointlike sources are likely themselves concentrated regions of hot gas. The morphology of the X-ray emission is similar to, but not identical with, UV and $H\alpha$ hot spots in the circumnuclear ring. The emission morphology can be understood if star formation is occurring through a series of instantaneous starbursts at various locations around the ring and the UV, $H\alpha$, and X-ray emission trace successively later stages in the evolution of the underlying stellar populations. X-ray emission extends at least 500 pc beyond the circumnuclear ring. This emission is interpreted as the result of gas outflow from the star-forming ring into the disk and halo of NGC 3351. There is evidence that the outflow is confined by cold ambient gas near the plane of the galaxy but that flow out of the plane is not restricted. The nucleus of the galaxy lacks both large amounts of hot gas and any pointlike source above an estimated X-ray luminosity of 10^{37} ergs s⁻¹ in the 0.5–8.0 keV band. This luminosity is orders of magnitude too low to account for the observed nuclear $H\alpha$ luminosity, 3.5×10^{38} ergs s⁻¹, by X-ray photoionization.

Subject headings: galaxies: individual (NGC 3351) — galaxies: starburst — galaxies: structure — X-rays: galaxies

1. INTRODUCTION

Central bars are a common feature of disk galaxies, occurring in at least half of the population. In early-type spirals, the asymmetric gravitational potential in the bar channels gas toward the center of the galaxy. Accretion stalls near the inner Lindblad resonance forming a circumnuclear ring of gas and dust (Buta & Combes 1996). The density of this gas increases until the ring becomes gravitationally unstable to collapse along its circumference and several giant gas clouds form (Elmegreen 1994). These clouds become hot spots of intense star formation. Presumably, once enough gas has been converted to stars, the cloud remnants are dispersed by stellar winds and supernovae. The entire process may repeat itself if accretion continues. Ultimately this depends on the stability of the bar itself, which can dissolve if the core mass exceeds $\sim 5\%$ of the total galaxy mass (Norman et al. 1996). The dynamics of these structures is critical to galactic bulge growth and hence evolution along the Hubble sequence (e.g., Wyse et al. 1997; Elmegreen 2005), to forming and sustaining central supermassive black holes (Wyse 2004; Ann & Thakur 2005), and to the physics behind the $M_{\text{BH}}-\sigma_*$ relation (Ferrarese & Merritt 2000).

NGC 3351 is an excellent example of a nearby (10.05 Mpc, $1'' = 49$ pc; Graham et al. 1997), early-type barred spiral galaxy with a star-forming circumnuclear ring (Fig. 1). The bar is ~ 4.6 kpc long and is surrounded by a 1 kpc wide inner ring. The circumnuclear ring is ~ 0.5 – 0.7 kpc in diameter and is characterized by a series of hot spots visible in UV (Colina et al. 1997), $H\alpha$ (Planesas et al. 1997; Bresolin & Kennicutt 2002), near-infrared (Elmegreen et al. 1997), and optical images.

We have obtained *Chandra* X-ray images of NGC 3351 in order to trace the effects of the circumnuclear ring, bar, and other structures on observed X-ray properties and to obtain a more complete multiwavelength picture of the star-forming process. Specifically, diffuse X-ray-emitting gas traces star formation in the disks (Tyler et al. 2004) and galactic winds in the halos (Wang et al. 2001; Strickland et al. 2004a, 2004b) of spiral galaxies, and we expect a similar correlation with the star-forming nuclear ring and inner ring in NGC 3351.

A description of the *Chandra* observations, data reduction methods, and properties of the discrete X-ray sources within NGC 3351 are presented in § 2. In § 3 we investigate the morphology of the X-ray emission (both diffuse and pointlike) in the circumnuclear region and compare it to star formation tracers observed at other wavelengths. We find that the likely source of X-ray emission from the circumnuclear ring is recent core-collapse supernovae (SNe) rather than stellar winds from young stars and that the SN rate needed to account for the X-ray properties is consistent with the recent star formation rate as deduced from the $H\alpha$ luminosity. We show that X-ray emission extends interior and exterior to the circumnuclear ring and that this emission is likely from an outflow—seen in projection—originating from the core of the galaxy. We discuss whether or not the outflow is confined and what implications this has on the dynamics and evolution of the nuclear region in § 4.

2. X-RAY OBSERVATIONS AND DATA ANALYSIS OF NGC 3351

Chandra Advanced CCD Imaging Spectrometer (ACIS) observations of NGC 3351 were obtained on 2005 February 8 (ObsID 5929), 2005 May 8 (5930), and 2005 July 1 (5931). The duration of each observation was approximately 39.5 ks, and the intervals between observations were 89 and 54 days, respectively. The location of the nucleus of NGC 3351 was offset $1'$ from the back-illuminated CCD S3 aim point in all observations to center the galaxy on the S3 detector. All observations were made in the full-frame timed

¹ Universities Space Research Association, NASA Marshall Space Flight Center, XD12, Huntsville, AL 35805.

² Department of Physics, University of Alabama, Huntsville, AL 35899.

³ Space Science Department, NASA Marshall Space Flight Center, XD12, Huntsville, AL 35805.

⁴ Harvard-Smithsonian Center for Astrophysics, 60 Garden Street, Cambridge, MA 02138.

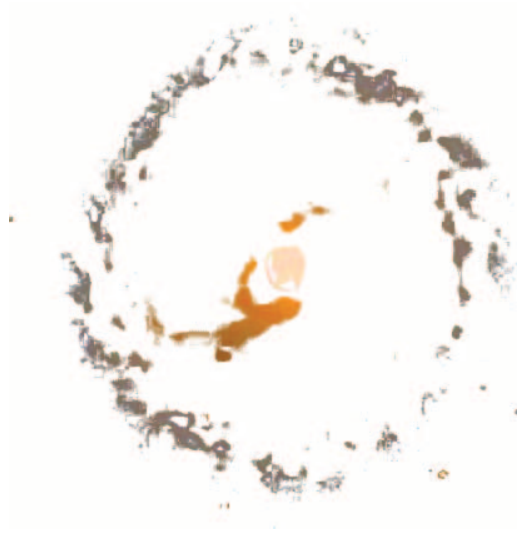


FIG. 1.—*Top*: Three-color optical image of NGC 3351 adapted from the Sloan Digital Sky Survey (blue, green, and red correspond to the g , r , and i bands, respectively). North is up, and east is to the left. The image covers a $5' \times 5'$ area. The nuclear region is overexposed but contains a circumnuclear ring (see Fig. 2). The nuclear region is surrounded by dark dust lanes that extend along the leading edge of the bar. The bar, appearing yellow in this image, is oriented at an angle $\sim 110^\circ$ east of north. The bar terminates at an inner ring (*blue with dark dust lanes*) of $\sim 65''$ radius (3.2 kpc). Spiral arms extend beyond the inner ring. *Bottom*: Color-selected regions from the top panel image chosen to show just the nuclear region, dust lanes, and inner ring.

exposure mode using the standard 3.2 s frame time, the standard ACIS-S imaging mode chip set, and the faint telemetry format.

Beginning with the Level 1 event lists, a CTI correction was applied and pixel randomization was removed (using the *Chandra* X-Ray Center's CIAO ver. 3.2.1 tool `acis_process_events`). The standard *ASCA* event grades were selected; a GTI filter was applied, and hot pixels, columns, and cosmic-ray afterglows were removed to produce the final event lists for analysis. Three brief, <400 s, flares were detected near the end of ObsID 5929 with count rates up to twice the mean background count rate over the entire observation. These were determined to have no impact on subsequent data analysis and were retained.

A fourth data set was constructed by co-adding the three individual observations using FTOOLS utilities.⁵ This requires a coordinate translation of two of the data sets to register them to the third data set and merging of the GTI extensions to produce the correct GTIs for the co-added data. The translations were computed from the relative positions of a bright source near the aim point that was detected in all three observations. As a check of the absolute source locations, we compared X-ray source positions to Two Micron All Sky Survey (2MASS) All-Sky Data Release catalog entries and found four sources with 2MASS counterparts. Positions of these sources are within 1 ACIS pixel ($0''.492 \text{ pixel}^{-1}$) of their 2MASS positions, and no further adjustments of the *Chandra* astrometry was made.

The central region of NGC 3351, the focus of the present study, is located near the center of the back-illuminated S3 CCD in all three observations. Changes in instrument response and spacecraft orientation among the three observations were determined to have minor effects on the X-ray data at this location. Therefore, the fourth (co-added) data set is used extensively in this work. Spectral response matrices and ancillary response files (generated using CIAO ver. 3.2.1 software, which accounts for contamination buildup) for the intermediate observation (ObsID 5930) were used in the analysis of the co-added data.

2.1. Discrete X-Ray Sources

Analysis of the discrete X-ray source population observed in the individual observations is presented elsewhere (D. A. Swartz et al. 2006, in preparation). Some of the X-ray properties of these sources are tabulated here for reference. Fifty-three discrete sources were detected within the optical extent of NGC 3351 above a signal-to-noise ratio of 2.4 and with at least a 4.5σ significance above local background. The optical extent of NGC 3351 was defined as the blue-light isophote at surface brightness level 25.0 mag s^{-2} (major diameter $D_{25} = 7''.41$). The 4.5σ significance was chosen after visual inspection of potential sources within the high-background nuclear region to ensure that all obvious pointlike sources were cataloged (normally, 5σ is used).

Table 1 lists the X-ray properties of these sources. Columns (1)–(3) contain a unique source name and source coordinates, listed in order of increasing right ascension (R.A.). Columns (4)–(6) contain the background-subtracted counts (with errors) detected in the co-added data set in three broad X-ray bands defined as *S* (0.3–1.0 keV), *M* (1.0–2.0 keV), and *H* (2.0–8.0 keV). Column (7) lists the 0.3–8.0 keV luminosities estimated assuming a $\Gamma = 1.7$ power-law photon index and the Galactic absorption column along the line of sight, $N_{\text{H}} = 2.8 \times 10^{20} \text{ cm}^{-2}$. Columns (8)–(9) list two measures of X-ray source variability: (a) Variability

during each observation estimated by constructing light curves, grouped into 2 ks bins, and performing χ^2 tests against the constant count rate hypothesis. None of the sources varied significantly according to this test ($\chi^2 \lesssim 40$ for 20 degrees of freedom [dof] or $\lesssim 3 \sigma$). Results of these tests are indicated in column (8) of Table 1 for the observation with the most significant variability. (b) Variability over the intervals *between* observations estimated by the statistical significance, σ_V , of the difference in the number of counts detected in the individual observations from the mean of all three observations. Several sources varied significantly between observations according to this test ($|\sigma_V| \gtrsim 3$). The largest value of $|\sigma_V|$ among the three observations for each source is listed in column (9) of Table 1.

2.2. Tests for the Pointlike Nature of the X-Ray Sources

The majority of the discrete X-ray sources detected in the NGC 3351 field are expected to be bright individual X-ray binaries (XRBs). Some SN remnants (SNRs) in NGC 3351, background active galactic nuclei, and foreground stars are also expected to be in the field. The nuclear region of NGC 3351 also contains substantial amounts of hot diffuse gas, and we analyze this region in detail in § 3. In order to do so, we made a careful evaluation of the sources within the circumnuclear region to distinguish between individual X-ray point sources and highly concentrated knots of hot gas that may appear pointlike in the X-ray images. Knots of hot gas should be relatively soft and steady X-ray sources and may appear extended at the resolution of *Chandra*.

The standard method used to test for source extent is to extract azimuthally averaged radial profiles of sources and compare them to the profiles of model point-spread functions (PSFs). The intensity and spatial inhomogeneity of the extended X-ray emission and the high density of sources in the nuclear region makes this technique impractical. Instead, we simultaneously fit circular Gaussian models to the observed distribution of events associated with the 12 sources in the inner $32'' \times 32''$ region of NGC 3351 (indicated by asterisks in Table 1) with additional (circular and elliptical) Gaussian models representing the underlying background structure in this region. The positions, Gaussian σ values, and normalizations were allowed to vary in the fitting. Sources in the nuclear region with $\sigma \gtrsim 0''.5$ are considered extended sources.

The results of this fitting and the observed X-ray colors and X-ray variability of the sources suggest that five of the sources in the nuclear region are likely XRBs. Three nonvariable sources are pointlike but are likely unresolved knots of hot gas based on their soft X-ray spectra. One source has a (soft) pointlike component above more extended emission, which is best modeled as multiple overlapping sources (with slightly offset centroids and different widths). The three remaining sources in the nuclear region are clearly soft, steady, and extended regions of thermal emission. The seven sources judged in this way to be hot gas knots rather than XRB-like point sources are designated by the prefix *k* in column (1) of Table 1.

3. CIRCUMNUCLEAR STAR FORMATION

The X-ray image of NGC 3351 was examined to search for the effects of the circumnuclear ring, bar, and inner ring on its X-ray properties. We found no significant enhancement of diffuse or discrete X-ray emission in the bar or inner ring relative to the surrounding regions. We therefore focus our analysis on the central region of NGC 3351 for the remainder of this work. The active circumnuclear region of NGC 3351 appears as the overexposed core in the image of Figure 1.

⁵ Available at http://heasarc.gsfc.nasa.gov/docs/software/ftools/ftools_menu.html.

TABLE 1
PROPERTIES OF THE X-RAY SOURCES IN NGC 3351

NAME (1)	R.A. (2)	DECL. (3)	S (0.3–1.0 keV) (4)	M (1.0–2.0 keV) (5)	H (2.0–8.0 keV) (6)	$L_X/10^{36}$ (ergs s $^{-1}$) (7)	TIMING	
							χ^2 (20 dof) (8)	σ_V (9)
s01.....	10 43 50.12	+11 40 33.76	-1.07 ± 1.10	11.2 ± 3.63	8.26 ± 3.67	13.6	17.0	3.3
s02.....	10 43 50.24	+11 42 48.16	0.63 ± 1.47	2.32 ± 1.75	7.52 ± 3.03	7.7	18.2	2.9
s03.....	10 43 50.66	+11 42 02.62	30.2 ± 5.67	38.4 ± 6.25	16.0 ± 4.26	62.6	28.2	1.7
s04.....	10 43 51.37	+11 42 39.04	10.4 ± 3.32	38.7 ± 6.25	20.0 ± 4.59	51.1	26.2	2.4
s05.....	10 43 52.34	+11 40 43.60	9.13 ± 3.34	3.41 ± 2.27	3.29 ± 2.50	11.7	20.0	6.3
s06.....	10 43 52.88	+11 42 24.06	36.6 ± 6.17	157.0 ± 12.5	154.0 ± 12.5	257.2	19.7	2.0
s07.....	10 43 53.67	+11 41 27.98	14.7 ± 4.02	3.46 ± 2.01	-0.74 ± 1.09	12.9	36.0	1.0
s08.....	10 43 53.82	+11 40 14.76	4.82 ± 2.47	20.4 ± 4.59	6.95 ± 3.03	23.8	29.0	4.2
s09.....	10 43 54.87	+11 41 17.99	-1.06 ± 1.05	2.94 ± 2.03	3.99 ± 2.49	4.3	23.5	3.5
s10.....	10 43 55.09	+11 44 02.90	8.38 ± 3.02	5.69 ± 2.46	12.4 ± 3.77	19.6	23.5	1.7
s11.....	10 43 55.27	+11 41 29.33	35.8 ± 6.10	49.3 ± 7.08	31.9 ± 5.86	86.6	38.5	1.5
s12.....	10 43 56.14	+11 42 04.54	2.08 ± 2.05	2.23 ± 1.75	1.98 ± 2.05	4.7	24.4	0.5
s13.....	10 43 56.30	+11 41 37.11	35.7 ± 6.09	37.5 ± 6.17	20.8 ± 4.70	69.6	21.1	0.7
s14.....	10 43 56.33	+11 43 48.85	-0.25 ± 1.01	1.63 ± 1.42	9.51 ± 3.17	8.1	27.5	1.2
s15.....	10 43 56.44	+11 42 20.81	4.92 ± 3.09	13.9 ± 3.74	5.87 ± 2.68	18.3	19.0	1.6
s16.....	10 43 56.45	+11 41 50.63	7.14 ± 2.84	6.62 ± 2.65	-1.14 ± 1.05	9.3	17.0	1.1
s17.....	10 43 56.54	+11 40 47.59	3.39 ± 2.01	2.12 ± 1.75	6.07 ± 2.86	8.6	19.0	2.7
s18*.....	10 43 56.72*	+11 42 50.31*	$25.6 \pm 5.10^*$	$45.8 \pm 6.78^*$	$12.4 \pm 3.61^*$	62.0*	29.5*	0.2*
s19.....	10 43 56.73	+11 42 22.18	31.8 ± 6.05	46.9 ± 6.86	38.8 ± 6.34	87.0	21.9	1.7
s20*.....	10 43 56.82*	+11 42 20.78*	$66.8 \pm 8.46^*$	$168.0 \pm 13.0^*$	$134.0 \pm 11.6^*$	272.9*	25.7*	0.7*
s21.....	10 43 56.85	+11 41 21.78	32.9 ± 5.84	2.42 ± 1.74	1.13 ± 1.44	27.0	27.4	1.4
s22.....	10 43 57.02	+11 44 47.04	1.21 ± 1.44	11.6 ± 3.47	6.71 ± 2.85	14.4	22.0	4.0
s23.....	10 43 57.10	+11 42 48.22	3.30 ± 2.01	3.77 ± 2.00	4.30 ± 2.25	8.4	19.0	2.2
s24*.....	10 43 57.36*	+11 42 12.08*	$67.5 \pm 9.55^*$	$39.7 \pm 6.79^*$	$14.3 \pm 4.00^*$	89.9*	24.0*	6.8*
k25*.....	10 43 57.42*	+11 42 12.88*	$94.5 \pm 10.9^*$	$55.7 \pm 7.88^*$	$12.3 \pm 3.74^*$	120.2*	25.4*	1.9*
k26*.....	10 43 57.62*	+11 42 17.26*	$94.5 \pm 10.9^*$	$32.7 \pm 6.25^*$	$2.28 \pm 2.00^*$	95.8*	36.6*	1.2*
k27*.....	10 43 57.62*	+11 42 06.80*	$134.0 \pm 12.5^*$	$63.7 \pm 8.37^*$	$11.3 \pm 3.61^*$	154.7*	29.7*	1.8*
s28*.....	10 43 57.72*	+11 42 24.23*	$10.2 \pm 3.70^*$	$17.5 \pm 4.26^*$	$8.06 \pm 3.04^*$	26.5*	28.0*	1.6*
s29.....	10 43 57.78	+11 45 07.76	-0.51 ± 1.03	9.28 ± 3.17	14.9 ± 4.01	17.5	27.8	2.3
k30*.....	10 43 57.79*	+11 42 17.89*	$56.8 \pm 8.55^*$	$20.7 \pm 5.00^*$	$1.82 \pm 1.73^*$	58.7*	31.1*	1.5*
k31*.....	10 43 57.92*	+11 42 09.05*	$77.8 \pm 9.70^*$	$23.7 \pm 5.29^*$	$1.82 \pm 1.73^*$	76.5*	24.0*	1.0*
s32*.....	10 43 57.93*	+11 42 22.17*	$22.0 \pm 5.08^*$	$26.5 \pm 5.21^*$	$15.0 \pm 4.03^*$	47.0*	18.9*	0.8*
k33*.....	10 43 58.11*	+11 42 16.51*	$64.5 \pm 9.39^*$	$28.7 \pm 5.92^*$	$5.28 \pm 2.65^*$	72.9*	31.7*	1.3*
k34*.....	10 43 58.15*	+11 42 03.57*	$15.5 \pm 6.27^*$	$9.75 \pm 4.01^*$	$5.28 \pm 2.65^*$	22.6*	22.0*	2.3*
s35.....	10 43 58.30	+11 41 33.38	-0.12 ± 1.04	4.70 ± 2.24	6.81 ± 2.84	8.4	27.5	0.3
s36.....	10 43 58.59	+11 41 48.09	15.2 ± 4.14	-0.20 ± 1.01	0.34 ± 1.47	11.4	20.0	2.9
s37.....	10 43 59.17	+11 42 43.99	13.8 ± 3.74	11.9 ± 3.46	9.22 ± 3.17	25.8	23.2	7.5
s38.....	10 43 59.41	+11 42 18.00	-0.21 ± 1.09	8.40 ± 3.02	4.94 ± 2.48	9.7	18.2	1.2
s39.....	10 43 59.45	+11 39 48.59	-0.03 ± 1.49	8.29 ± 3.01	6.63 ± 3.38	11.0	38.0	0.6
s40.....	10 43 59.48	+11 42 09.39	4.02 ± 2.27	14.9 ± 3.88	31.0 ± 5.67	36.9	23.8	0.9
s41.....	10 43 59.51	+11 43 15.47	44.7 ± 6.71	32.4 ± 5.75	7.48 ± 2.84	62.6	25.0	2.2
s42.....	10 43 59.54	+11 42 07.15	111.0 ± 10.6	177.0 ± 13.3	147.0 ± 12.2	321.9	26.3	0.5
s43.....	10 43 59.72	+11 42 29.63	16.7 ± 4.12	5.90 ± 2.45	4.51 ± 2.24	20.1	20.0	6.9
s44.....	10 44 00.00	+11 41 32.92	4.42 ± 2.25	7.35 ± 2.84	0.49 ± 1.45	9.1	18.2	0.9
s45.....	10 44 00.22	+11 40 03.99	1.37 ± 1.77	4.99 ± 2.47	5.97 ± 3.21	9.1	27.5	1.0
s46.....	10 44 00.28	+11 41 51.84	26.2 ± 5.20	56.6 ± 7.55	48.0 ± 7.01	96.8	25.6	1.9
s47.....	10 44 01.73	+11 41 51.84	8.04 ± 3.02	8.52 ± 3.01	2.89 ± 2.28	14.4	19.0	2.7
s48.....	10 44 02.65	+11 42 54.28	7.87 ± 2.83	1.96 ± 1.41	-0.36 ± 1.01	7.0	19.0	0.6
s49.....	10 44 03.35	+11 40 37.32	-0.16 ± 1.50	10.6 ± 3.49	14.5 ± 4.29	18.5	26.2	2.8
s50.....	10 44 04.12	+11 43 04.07	9.56 ± 3.17	-0.29 ± 1.02	0.84 ± 1.47	7.5	29.0	1.5
s51.....	10 44 05.23	+11 41 33.74	1.23 ± 1.44	1.56 ± 1.43	4.45 ± 2.48	5.4	27.5	1.4
s52.....	10 44 06.45	+11 44 31.11	26.7 ± 5.30	9.57 ± 3.17	0.49 ± 1.45	27.2	29.1	2.3
s53.....	10 44 07.14	+11 41 44.19	2.77 ± 2.03	2.66 ± 1.74	4.09 ± 2.49	7.0	27.5	0.4

NOTES.—Cols. (1)–(3): Unique source name and sky position in J2000.0 coordinates. Units of right ascension are hours, minutes, and seconds, and units of declination are degrees, arcminutes, and arcseconds. An “s” in the source name denotes a point source; “k” denotes a concentration or knot of hot gas. Cols. (4)–(6): X-ray source counts after background subtraction for the co-added data. Col. (7): X-ray luminosity in the 0.3–8.0 keV band assuming a $\Gamma = 1.7$ power-law spectrum absorbed by the Galactic column of $N_H = 2.8 \times 10^{20} \text{ cm}^{-2}$ and adopting the Cepheid distance to NGC 3351 of 10.05 Mpc (Graham et al. 1997). Cols. (8)–(9): Measures of X-ray variability (see text).

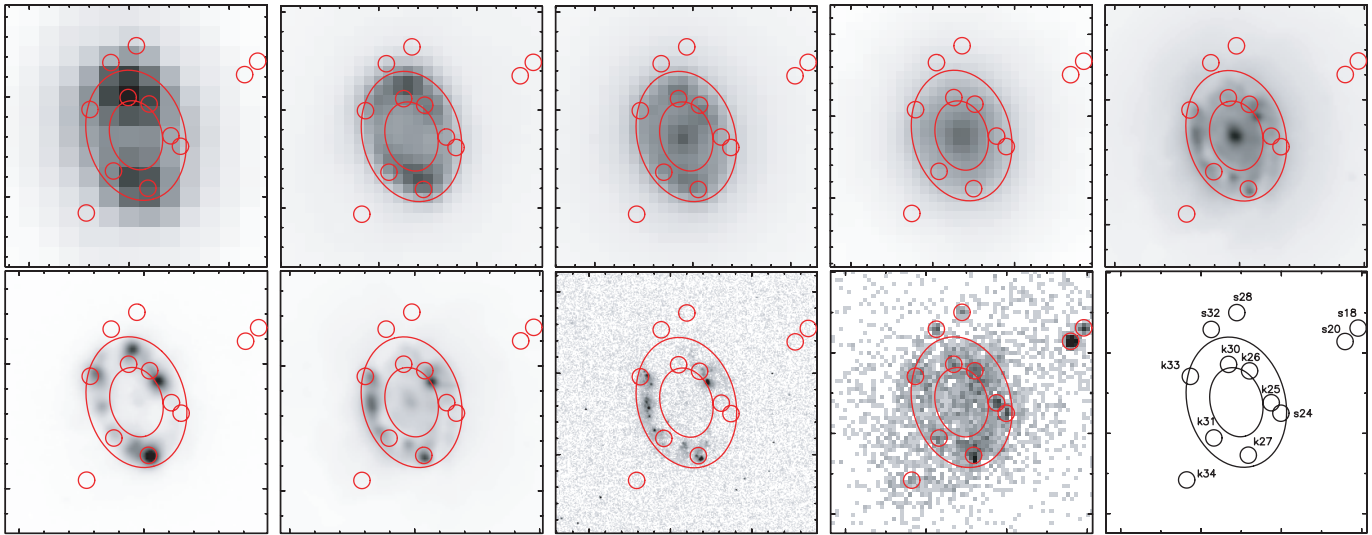


FIG. 2.—Images of the central $32'' \times 32''$ region of NGC 3351. *Top, left to right:* *Spitzer* MIPS 24, IRAC 5.8, and IRAC $4.6 \mu\text{m}$; 2MASS *J*; and CTIO 4.0 m Mosaic2 *I*. *Bottom, left to right:* CTIO 4.0 m Mosaic2 continuum-subtracted $H\alpha$ and *B*; *Hubble* F218W; and *Chandra* 0.5–8.0 keV. The last panel identifies the sources using the unique names given in Table 1. Circles are $1''$ in radius and denote X-ray source positions. Ellipses denote the circumnuclear ring (see text for details).

3.1. General Morphology

The circumnuclear star-forming region of NGC 3351 appears as an elliptical ring of hot spots at wavelengths shortward of the *I* band (Fig. 2). The emission at infrared wavelengths, in contrast, is dominated by light from late-type stars and is concentrated at the galactic nucleus, although there is some structure associated with the ring visible in higher resolution images (cf. Elmegreen et al. 1997). At the longer wavelengths sampled by *Spitzer* and in the CO bands (see Devereux et al. 1992; Planesas et al. 1997) the emission is localized to two lobes near the extrema of the ring major axis.

We parameterized the circumnuclear ring as an elliptical annulus with a Gaussian cross section fitted to the highest resolution data available: the *Hubble* F218W UV image. When constrained to be centered on the nucleus, the best-fit position angle of this model is nearly perpendicular to the bar axis. This is expected if the ring traces the x_2 orbits perpendicular to the bar (Contopoulos & Papayannopoulos 1980). Therefore, we constrained the position angle to be P.A. = 15° east of north (cf. Buta 1988). With these two constraints the ring semimajor axis is $a = 300$ pc and the major-to-minor axis ratio is $a/b = 1.35$. Because of azimuthal inhomogeneities along the ring circumference, we do not consider the derived width of the Gaussian ring cross section to have particular physical significance, but it is convenient to choose a ring half-width of $r \sim 100$ pc to delineate the various regions of the star formation zone in the discussion that follows. The ring model along with $1''$ radius circles denoting the positions of all the detected X-ray sources are overlaid on the images of Figure 2.

In addition to the circumnuclear ring, dust lanes are visible along the leading edge of the bar (rotation is counterclockwise; Buta 1988; Rubin et al. 1975) that terminate near the extremities of the major axis of the circumnuclear ring (see Fig. 1). The dust lane along the eastern arm of the bar is stronger and is closer to the observer than the dust lane on the western arm. The eastern dust lane is connected to a shorter dust lane that extends clockwise from the southern end of the ring toward the northeast. There is an abrupt edge to the circumnuclear emission that appears to be coincident with this dust feature. This is most clearly seen in the X-ray image of Figure 2 but is present in high-contrast *B*, *V*, and $H\alpha$ images as well.

3.2. X-Ray Morphology and Spectrum

The X-ray emission follows roughly the morphology seen at *I* through UV. It is composed of several pointlike features on the ring with additional diffuse emission both inside and outside of the ring. The emission outside the ring extends to about 800 pc from the nucleus to the northwest and to the southeast.

Figure 3 displays the central $32'' \times 32''$ region of NGC 3351. The left panel is a true-color image of the X-ray intensity showing the extension of the diffuse emission and indicating that the pointlike concentrations or knots on the ring have similar spectral properties as the more extended diffuse emission: namely, a soft spectrum indicative of hot gas. The center panel is a composite of X-ray (*blue*), UV (*green*), and $H\alpha$ (*red*) images showing that the emission features at different wavelengths are not necessarily coincident. Regions emitting in all three wave bands appear as bright white regions. The right-hand panel displays the X-ray spectral hardness ratio $(H - S)/T$ where $T = S + M + H$ (§ 2.1) showing that most of the emission is soft (red in the figure) including the pointlike sources judged to be knots of hot gas in contrast to the hard XRB sources, which appear blue. Several small regions also appear blue, indicating relatively hard spectral colors. These may be weak XRBs below the detection limit or simply Poisson noise. The more extended hard color region near the north end of the ring major axis is likely a region of high absorption as this region also has high *J–K* colors and has low surface brightness (indicating absorption) in the optical images (Fig. 2).

For analysis of the hot gas component of the star-forming regions of NGC 3351, we consider three spatial components: the ring, the region interior to the ring, and the region exterior to the ring above a surface brightness of 0.5 X-ray events per pixel in the 0.3–3.0 keV band. The boundaries of these regions are shown in the hardness ratio plot of Figure 3. The spectrum of each region was extracted from the co-added data after excluding the sources labeled “s” in Table 1 (see Fig. 2), as these are all likely XRBs. A background spectrum was chosen in a region away from the circumnuclear source region but not too close to the edge of the CCD array where the additional absorption due to molecular buildup on the ACIS filter is highest. We confine our analysis to the 0.3–3.0 keV energy range because there is no measurable flux above

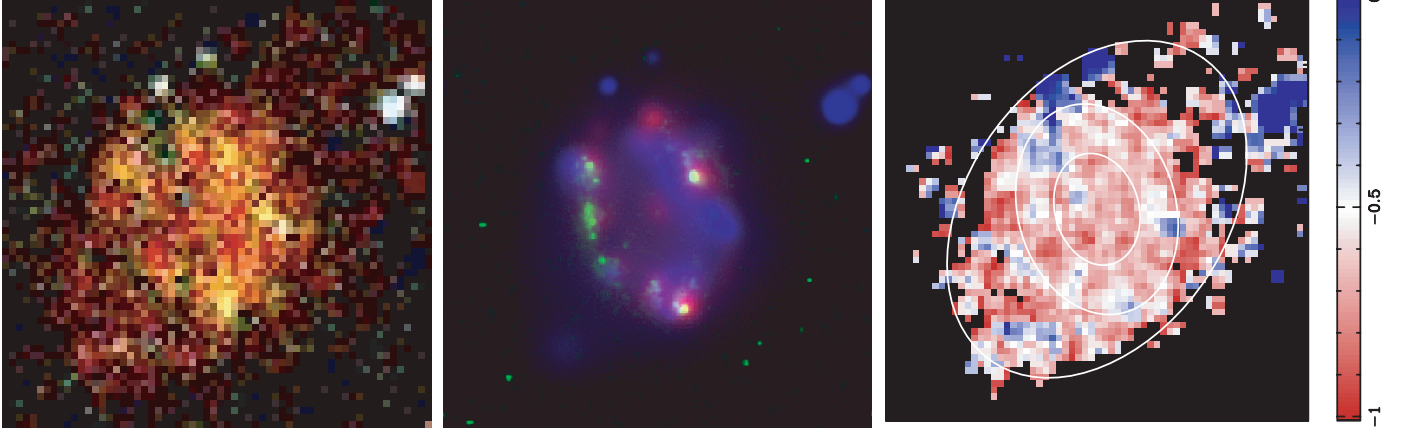


FIG. 3.—*Left*: True-color X-ray image of the central $32'' \times 32''$ region of NGC 3351. Red, green, and blue colors sample the S , M , and H bands (§ 2.1). *Center*: Combined X-ray (blue), $H\alpha$ (red), and UV (green) image of the same region. The X-ray image has been smoothed using the CIAO tool `csmooth`. *Right*: X-ray hardness ratio $(H - S)/T$ of the same region. Blue denotes relatively high spectral hardness (color bar depicts scale: ratio $\rightarrow -1$ as $S \rightarrow T$). Pixels in the smoothed image with fewer than 0.5 counts appear dark.

3.0 keV in the diffuse source spectra and the detector background is high below 0.3 keV.

The spectra were fitted with a variety of models representative of thermal plasmas or thermal plasma plus power-law components (representing hot gas and unresolved XRBs, respectively) using the XSPEC analysis tool. All models required a low hydrogen column density; we thus constrained this parameter to be equal to or exceed the Galactic value, $N_H = 2.8 \times 10^{20} \text{ cm}^{-2}$, in all trials. Results of the best-fitting single-temperature absorbed VMEKAL models for the three spatial regions are listed in Table 2 (errors are 90% confidence ranges for a single interesting parameter). This is the best-fitting model to the observed spectra. In particular, neither a power-law component nor multiple thermal components are required by the data. The observed spectrum and best-fitting model for the three regions are shown in Figure 4.

The results of the spectral fits show the three regions have similar X-ray temperatures, as can be deduced qualitatively from

TABLE 2
DIFFUSE PLASMA PROPERTIES

Parameters	Interior	Ring	Exterior
Fit Parameters			
Source counts.....	657	1725	1328
N_H (10^{20} cm^{-2})	2.8	$4.7^{+4.5}_{-3.4}$	2.8
T_e (MK)	$6.8^{+0.6}_{-1.5}$	$6.7^{+0.5}_{-0.9}$	$6.7^{+0.3}_{-1.0}$
Normalization ^a	$3.2^{+1.0}_{-0.9}$	$8.5^{+5.6}_{-2.8}$	$8.5^{+0.7}_{-1.6}$
O^b	$0.14^{+0.28}_{-0.14}$	$0.39^{+0.26}_{-0.21}$	$0.28^{+0.17}_{-0.10}$
Mg	0.17 ± 0.17	$0.60^{+0.41}_{-0.26}$	$0.21^{+0.15}_{-0.11}$
Si	$0.27^{+0.64}_{-0.23}$	$0.39^{+0.31}_{-0.22}$	$0.03^{+0.16}_{-0.03}$
Fe	$0.18^{+0.08}_{-0.06}$	$0.15^{+0.06}_{-0.05}$	$0.10^{+0.03}_{-0.01}$
$L_X/10^{38} \text{ ergs s}^{-1}$	2.5	6.5	5.0
Derived Parameters ^c			
V [f] (10^{63} cm^3)	1.1	1.5	38.3
n_e [$f^{-1/2}$] (cm^{-3})	0.19	0.26	0.05
P/k [$f^{-1/2}$] (10^5 K cm^{-3})	26.0	35.0	6.7
M_* [$f^{+1/2}$] ($10^5 M_\odot$)	2.5	4.5	22.9
E_{th} [$f^{+1/2}$] (10^{53} ergs)	6.0	10.8	54.3
t_c [$f^{+1/2}$] (Myr)	77	53	348

^a $K = (10^{-9}/4\pi D^2) \int n_e n_p dV$ (see text).

^b Abundance relative to solar values from Anders & Grevesse (1989).

^c Volume filling factor scaling in brackets (see text).

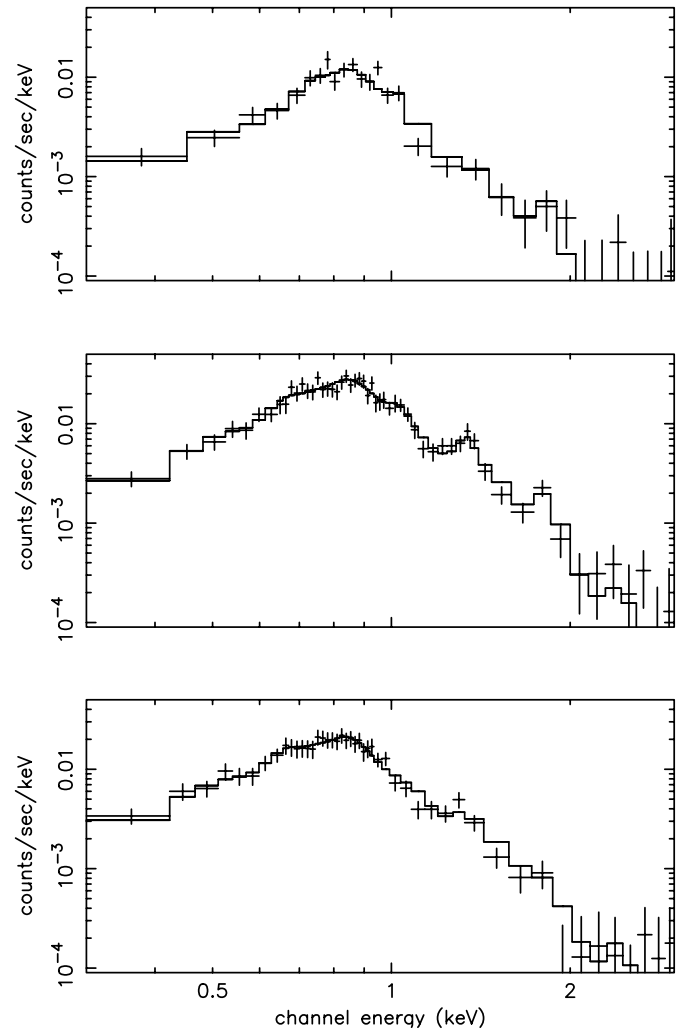


FIG. 4.—X-ray spectrum and best-fitting absorbed VMEKAL model (solid line) from the region interior to the circumnuclear ring (top), within the ring (middle), and exterior to the ring (bottom). Fit parameters are listed in Table 2. For display purposes, up to 10 adjacent energy bins have been combined to achieve a significant detection at least as large as 5σ .

inspection of the left panel of Figure 3. The bulk of the X-ray flux, however, comes from the circumnuclear ring. The highest abundances relative to solar are for the low- Z metals indicative of enhancement by core-collapse SNe. There may be a slight enhancement of these intermediate-mass elements in the ring relative to the other two regions considered, but the uncertainties are large.

The spectral model normalization parameter, K , is proportional to the emission integral, $\int n_e n_H dV \sim n_e^2 fV$, where the integral is over a volume, V , f represents a volume filling factor such that the actual volume occupied by X-ray-emitting gas is fV , and the assumption has been made that the ion and electron number densities n_i and n_e , respectively, are equal, which is roughly true for a hydrogen-dominated hot plasma with $n_i \sim n_H$. Hence, the electron density in the X-ray-emitting gas can be derived from the spectral model normalizations and knowledge of the emission geometry.

We assume that the ring is a circular torus of volume $V_r = 2\pi^2 ar^2$ and that the region interior to the ring is a sphere of volume $V_i = (4/3)\pi(a-r)^3$ using the ring parameters of § 3.1. The geometry is more uncertain for the region exterior to the ring. If the emission is extended above the bulge of the galaxy, as may be the case (§ 3.4), then the volume may be quite large. For simplicity, however, we represent it as an oblate spheroid defined by the ellipse that most closely matches the surface brightness contour at 0.5 events per pixel: $R = 780$ pc is the semimajor axis, and the major-to-minor axis ratio is 1.43. The volume of the emission region exterior to the ring is then $V_o = (4/3)\pi R^2(0.7R) - V_r - V_i$.

From n_e and the flux-weighted mean temperatures T_e we can estimate the hot gas pressure $P/k = 2n_e T_e$, mass $M_x = n_e \mu m_p V$, where m_p is the proton mass and $\mu = 1.4$ is the mass per proton, thermal energy $E_{th} = 3n_e V k T_e$, and the cooling time $t_c = E_{th}/L_X$ of the X-ray-emitting plasma as listed in Table 2. These derived quantities are all functions of the volume filling factor as indicated in Table 2.

3.3. The Circumnuclear Ring

The most intense recent star formation in NGC 3351 is traced by the $H\alpha$ emission in the circumnuclear ring. The X-ray data are used in this section to help constrain the age of the star formation activity and the mass involved in the star formation process.

Bresolin & Kennicutt (2002) estimated the age of the $H\alpha$ hot spots at 6 Myr from $H\beta$ and $He\text{ I } \lambda 5876$ equivalent widths assuming instantaneous bursts of star formation. Colina et al. (1997) found ages of 4–5 Myr for the entire circumnuclear region from *IUE* spectra. On the other hand, Planesas et al. (1997) estimated the total ionizing flux responsible for the hot spots to be $\sim 10^{53}$ photons s^{-1} . Such a high flux level is only produced within the first ~ 2 Myr after a starburst (Sternberg et al. 2003) because the massive early O stars supplying the flux quickly die off in SN explosions. The ionizing flux could be sustained for longer periods if star formation is continuous at a rate of $\sim 0.4 M_\odot \text{ yr}^{-1}$ (Sternberg et al. 2003). Planesas et al. (1997) estimated the total star formation rate in the $H\alpha$ hot spots is $0.25 M_\odot \text{ yr}^{-1}$.

The X-ray emission in the star-forming region is predominantly produced by SNe interacting with the ionized shells formed by massive star winds (Weaver et al. 1977; Chu & Mac Low 1990; Shull & Saken 1995). Thus, the X-ray emission traces a slightly later phase of the evolution of a starburst, ~ 10 Myr, when the many late O and B stars are dying off. Individual SNe can be copious X-ray emitters (e.g., Immler & Lewin 2003), but the emission is a sensitive function of the ambient conditions in which the SNR forms. From the X-ray emission, we estimate the

thermal energy in the ring is $\sim 10^{54}$ ergs. If 10^{51} ergs of kinetic energy is released by each SN, then of order 1000 SN events are needed to produce the thermal energy assuming a high conversion efficiency. At an age of ~ 4 –6 Myr, only stars more massive than about $40 M_\odot$ have become SNe. For a Salpeter IMF with an upper-mass cutoff of $100 M_\odot$, roughly 1400 stars more massive than $40 M_\odot$ are produced in a starburst of total mass $10^6 M_\odot$ (Leitherer et al. 1999). The thermal emission can therefore be accounted for by SNe from massive stars in a starburst of total mass $\sim 10^6 M_\odot$. If the stars in the X-ray-emitting regions are older than 4–6 Myr, then stars less massive than $40 M_\odot$ are also contributing to the SNe population and a starburst of less mass is required (or, equivalently, a lower efficiency converting kinetic to thermal energy is needed).

The actual conditions in the circumnuclear ring are probably intermediate between the instantaneous starburst and the continuous star formation scenarios: the fact that the $H\alpha$ and X-ray hot spots are not colocated and that they measure different but overlapping stages in the starburst evolution suggests that they are not coeval. If star formation in the ring is triggered by fragmentation into collapsing clouds driven by gravitational instabilities (Elmegreen 1994), then it is natural to expect some cloud-to-cloud variation in their physical properties and hence some variation in the onset and evolution of their star formation processes.

3.3.1. X-Ray Hot Spots

We can compare the properties of the individual $H\alpha$ hot spots to those of the X-ray knots. Planesas et al. (1997) estimated the mass of gas in several hot spots from the observed $H\alpha$ luminosity and assuming an electron density of 250 cm^{-3} . These masses range from 5×10^3 to $4 \times 10^4 M_\odot$ for a total mass of $3.5 \times 10^5 M_\odot$ in the $H\alpha$ -emitting ring gas. The conditions in the individual X-ray-emitting knots can be estimated by scaling from the mean density in the ring as derived from the X-ray spectrum: the density in the k th knot is then $n_k^2 = n_e^2 (f/f_k)(V/V_k)(C_k/C)$, where C is the number of X-ray counts and it is assumed the knots and the surrounding gas have the same plasma temperature. Assuming the knots are spherical with radii equal to the Gaussian half-widths deduced from our source fitting as described in § 2.2 and that the number of counts in the knots is given by the Gaussian normalizations,⁶ then the derived properties of the knots are as listed in Table 3. (Source k34 is not on the ring and is not included in Table 3.)

The masses of the X-ray knots are similar to the $H\alpha$ hot spot masses, but the pressures are several times higher ($H\alpha$ hot spot pressures are $P/k \sim 5 \times 10^6 \text{ K cm}^{-3}$ for temperatures of 10^4 K and densities 250 cm^{-3}). This again suggests that the principal difference between $H\alpha$ hot spots and X-ray knots is the age of their starbursts. The older X-ray-emitting regions are being powered by SNe, and the resulting overpressures will force hot tenuous gas away from surrounding cold, dense regions of the ring. The thermal energies of the individual knots are of order 10^{52} ergs, implying of order 10 SNe power each hot spot.

Another source of X-ray emission in the ring (and elsewhere) is accretion onto compact objects. There is one bright and variable X-ray source, s24, detected in the circumnuclear ring. The source luminosity is $\sim 10^{38} \text{ ergs s}^{-1}$ at its peak. Such high luminosities imply high accretion rates, which occur in Roche lobe overflow systems when the companion ascends the giant branch.

⁶ For sources with multiple Gaussian components, the largest σ model value is given, and the number of counts listed is the sum over all components. See § 2.2.

TABLE 3
X-RAY PROPERTIES OF CIRCUMNUCLEAR HOT SPOTS

Source Number	Radius (arcsec)	Volume (10^{60} cm^{-3})	Counts	n_e (cm^{-3})	P/k (10^7 K cm^{-3})	M_X ($10^3 M_\odot$)	L_X ($10^{37} \text{ ergs s}^{-1}$)	E_{th} (10^{51} ergs)
k25.....	0.4	0.9	65.9	2.1	2.8	2.2	2.5	5.2
k26.....	0.6	3.1	62.4	1.1	1.5	4.0	2.4	9.5
k27.....	1.0	14.2	278.0	1.1	1.5	18.3	10.6	43.3
k30.....	0.8	7.3	94.1	0.9	1.2	7.7	3.6	18.2
k31.....	0.3	0.4	27.3	2.0	2.7	0.9	1.0	2.2
k33.....	1.3	31.2	187.6	0.6	0.8	21.9	7.2	51.9
Total:	55.0	27.3	...

Statistically, the companion is probably a late O or B star (as there are more of these stars available and they spend longer periods off the zero-age main sequence than do more massive stars). Thus, the age of the variable XRB source on the ring is of order 10–50 Myr for a B0–B3 companion, and it represents a later phase in the evolution of the ring compared to the X-ray hot spots.

Grimm et al. (2003) have empirically estimated the X-ray luminosity and number of bright high-mass XRBs as a function of (continuous) star formation rate. For the rate of $0.25 M_\odot \text{ yr}^{-1}$ in the circumnuclear ring (Planesas et al. 1997), Grimm et al. predicted 1–2 XRBs with luminosity $>10^{38} \text{ ergs s}^{-1}$ and 5–8 with luminosity $>10^{37} \text{ ergs s}^{-1}$. We only detect the one (variable) XRB in the circumnuclear ring at $\sim 10^{38} \text{ ergs s}^{-1}$, but there could be several weak sources near (but not much above) $10^{37} \text{ ergs s}^{-1}$ that have escaped detection. Thus, the number of XRBs detected in the ring is consistent with expectations for continuous star formation at a moderate rate.

3.4. X-Ray Emission External to the Ring

In contrast to the emission from the circumnuclear ring, there are no indications of current or recent star formation accompanying the X-ray emission from regions exterior to the ring. Here we show that the most likely source of this emission is an outflow from the ring itself.

Outflow or breakout from pressure-confined regions into the halos of spiral and starburst galaxies is a common phenomenon (e.g., Strickland et al. 2002, 2004a; Tyler et al. 2004; Wang 2005). When viewed edge-on, galactic outflows are rather tenuous with the surface brightness decreasing exponentially with increasing height above the galaxy plane. The outflow may be confined by ambient halo material (which may be accumulated gas from earlier outflows) as in, e.g., NGC 3077 (Ott et al. 2003) or may be escaping into the intragalactic medium as in strong starburst systems (Strickland et al. 2004a, 2004b).

The 40° inclination of NGC 3351 makes it difficult to assess whether the observed emission is confined to the plane of the galaxy or extends significantly above it. Inspection of Figure 3 suggests a sharp edge to the distribution of X-ray emission southeast of the circumnuclear ring but a more gradual decrease in the surface brightness to the northwest. If the emitting gas is rising out of the circumnuclear ring in a conical pattern, the sharp feature could be tracing the edge of the cone of material expelled nearly along our line of sight, whereas the movement of material from the far side of the ring is more nearly perpendicular to our line of sight. This is shown schematically in Figure 5.

On the other hand, there is a dark region to the southeast of the circumnuclear ring visible in the Sloan image of Figure 1. This feature is likely a dust lane in or near the plane of the galaxy. The edge of this dust lane coincides with the sharp edge in the X-ray surface brightness distribution, implying that the X-ray emission

is from material confined by this dust. The fact that this dust lane extends counterclockwise from the dust lane along the leading edge of the bar suggests it may have formed out of the outflowing gas as it cooled instead of being entrained along the leading edge of bar orbits. The lack of significant absorption affecting the X-ray spectrum (§ 3.2) means that there is little or no cold material above the X-ray-emitting outflow.

We extracted a radial profile of the diffuse emission, centered on the nucleus, after omitting discrete sources and fitted exponential and power-law models to the data. The best-fitting model is an exponential, $\propto \exp(-r/H)$, where $H \sim 170 \text{ pc}$ is the scale length, resulting in a goodness of fit $\chi^2 = 113.1$ for 87 dof. For comparison, the best-fitting power law has $\chi^2 = 120.9$ for 87 dof for an index of -2.9 .

Strickland et al. (2004a) argued that an exponential profile (perpendicular to the plane) indicates a galactic fountain model for halo gas, i.e., the X-ray surface brightness profile follows the underlying density distribution and the hot gas is filamentary in structure. In contrast, models with emission from a volume filling component such as occurs if substantial mass is injected into the halo by the outflow (e.g., Suchkov et al. 1996) produce power-law X-ray surface brightness profiles with index ~ -3 (Chevalier & Clegg 1985).

3.5. X-Ray Emission Internal to the Ring (the Nucleus)

As with the region exterior to the ring, we surmise the bulk of the X-ray emission observed interior to the ring originated in the ring and traces an outflow.

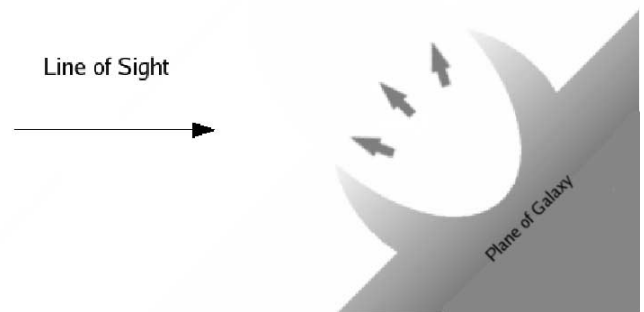


FIG. 5.—Schematic representation of a possible outflow geometry for NGC 3351. The galaxy is viewed from the left at an inclination of 40° , and the plane of the galaxy is perpendicular to the page. A conical flow of hot gas out of the plane is depicted by arrows. Cold gas within the plane of the galaxy is shown with heavy shading (only one face of the galaxy is shown). Outflow material that has cooled and condensed out of the flow could be falling back onto the disk. This is depicted as shaded regions on the edge of the outflow cone. The lack of X-ray-absorbing material along our line of sight suggests there is little or no cold material above the X-ray-emitting outflow.

There is little evidence of concentrated star formation in this region. The surface brightness at near-infrared wavelengths does peak at the center of the galaxy, but this emission traces the older underlying bulge population of stars. There is a modest amount of $H\alpha$ emission at the center, which could indicate a buildup of gas there. Planesas et al. (1997) estimated that the mass of $H\alpha$ -emitting gas at the center of the galaxy is $5000 M_\odot$. How this gas is excited is unclear. There is no evidence for heating by young stars in situ. Possibly, gas escaping the ring but still confined to the bulge gravitational potential is converging at the nucleus and being reheated by shocks. Another explanation is a nuclear supermassive black hole is exciting its surroundings.

No individual X-ray sources are detected interior to the ring. The 90% confidence upper limit to the X-ray emission from the nucleus is $L_X = 5.5 \times 10^{36}$ ergs s^{-1} in the 0.5–8.0 keV band, assuming a $\Gamma = 1.7$ power-law index and the Galactic column density of 2.8×10^{20} cm^{-2} . This estimate allows for uncertainty in the registration of the X-ray image and in the absolute position of the nucleus by assuming the brightest pixel in a $2''$ radius about the nominal center of NGC 3351 is the nucleus and using a $1''$ source extraction radius.

The Sloan Digital Sky Survey obtained an optical spectrum of the nucleus of NGC 3351. It shows Balmer emission lines but lacks most other features characteristic of active galactic nuclei. From the continuum shape of this spectrum and from the 2MASS J – K colors, we estimate the extinction in the nucleus of NGC 3351 to be $E(B-V) \sim 0.3$. This corresponds to a hydrogen column density of 2×10^{21} cm^{-2} or about 10 times the Galactic value. This would increase the estimated X-ray upper limit luminosity to 7×10^{36} ergs s^{-1} and the unabsorbed (intrinsic) X-ray luminosity to about 10^{37} ergs s^{-1} . For comparison, Planesas et al. (1997) estimated the $H\alpha$ luminosity at the center of the galaxy as 3.5×10^{38} ergs s^{-1} . Thus, the $H\alpha$ emission from the nuclear region is far more than can be accounted for by X-ray photoionization.

Dong & De Robertis (2006) estimated that the central mass concentration in NGC 3351 is $\sim 10^7 M_\odot$ using the correlation between M_{BH} and K -band luminosity (after rescaling to a distance of 10 Mpc to NGC 3351). This is consistent with the estimate of Sarzi et al. (2002) from measured emission-line widths using the M_{BH} – σ_* relation and the estimate from the correlation between M_{BH} and the Sersic index of the optical surface brightness profile (Graham et al. 2003).

The Bondi rate of accretion of hot gas ($kT \sim 0.5$ keV) for an object of this mass is $\dot{M}_B \sim 2 \times 10^{-5} (n_e/cm^{-3}) M_\odot$ yr^{-1} or about 10^{-4} of the Eddington accretion rate \dot{M}_{Edd} . The hot gas density in the nuclear region was estimated in § 3.2 as $n_e \sim 0.2 f^{-1/2}$ cm^{-3} . Assuming a 10% radiative efficiency, the luminosity expected from Bondi accretion is therefore $L = 0.1 \dot{M}_B c^2 \sim 3 \times 10^{40}$ ergs s^{-1} or $\sim 2 \times 10^{-5}$ of the Eddington luminosity, L_{Edd} . If, instead, accretion is advection dominated, then the radiative efficiency is much lower and the accretion rate may be an order of magnitude lower than the classical Bondi rate (Narayan 2002). From the self-similar solution of Narayan & Yi (1994), we expect a nuclear luminosity $\sim (M_B/\dot{M}_{Edd})^2 L_{Edd} \sim 10^{-8} L_{Edd} \sim 10^{37}$ ergs s^{-1} . A similar order-of-magnitude estimate for the intrinsic nuclear X-ray emission can be obtained from the more detailed advection model of Merloni et al. (2003).

There is also warm ($H\alpha$ -emitting) and cold gas present in the core of NGC 3351. Planesas et al. (1997) estimated that the $H\alpha$ luminosity at the center of the galaxy as 3.5×10^{38} ergs s^{-1} . We estimate that the size of the $H\alpha$ emission region is $\lesssim 30$ – 50 pc from the $H\alpha$ image, i.e., at or below the limit of resolution. Thus, the density of warm gas is at least $n_e = 8$ cm^{-3} . Planesas et al.

(1997) estimated an H_2 mass of $3.5 \times 10^8 M_\odot$ within 700 pc of the center of NGC 3351 from radio measurements of CO $2 \rightarrow 1$ emission. Devereux et al. (1992) obtained about half this value for the molecular mass within the circumnuclear ring of NGC 3351, a region of equivalent area as sampled by Planesas et al. (1997). The mean number density of molecular gas within an oblate spheroid of dimensions 900×300 pc (following Devereux et al. 1992) is then $7 H_2$ cm^{-3} . However, the CO emission morphology is similar to the far-infrared emission shown in Figure 2; namely, it is concentrated in two regions near the ends of the ring major axis. Thus, we estimate the molecular gas density at the nucleus to be $\sim 10\%$ of the mean (consistent with our estimated extinction toward the nucleus)⁷ or 0.35 – $0.70 H_2$ cm^{-3} .

Thus, the amount of material available for accretion onto any compact object at the core of NGC 3351 is substantial. The observed upper limit to the X-ray luminosity from the nucleus implies the radiative efficiency of this accretion must be extremely low (consistent with the prediction of advection-dominated accretion flow models) and the accretion rate must be $\lesssim 10\%$ of the classical Bondi rate.

4. DISCUSSION

We have analyzed the X-ray emission from the central region of NGC 3351. The general picture that emerges is that X-rays are produced in regions of intense recent star formation within a circumnuclear ring and that some hot gas is escaping into surrounding regions.

The circumnuclear ring is also a strong $H\alpha$ and UV emitter. The emission morphology can be understood if star formation is occurring through a series of instantaneous bursts at various locations around the ring with differing amounts of extinction. Then the UV, $H\alpha$, and X-ray emission trace different stages in the evolution of the underlying stellar populations beginning with UV and $H\alpha$ emission from the youngest and most massive stars and culminating in SN-powered X-ray emission about 10 Myr after the starbursts. This explains the general lack of spatial coincidence among individual UV, $H\alpha$, and X-ray hot spots if they were formed at different times and the UV hot spots are relatively unobscured. The few regions that are radiating strongly in all three wave bands are probably undergoing a more extended star formation episode lasting of order 10 Myr or longer.

Of order 1000 SNe are needed to produce the X-ray luminosity emanating from the ring. Since the cooling timescale of this gas is long, $50 f^{1/2}$ Myr (where f is the volume filling factor), the SN rate need only be $2 \times 10^{-5} f^{-1/2}$ yr^{-1} . This is easily maintained by continuous star formation at a rate of 0.25 – $0.40 M_\odot$ yr^{-1} or (after about 10 Myr) by a starburst of $\sim 10^6 M_\odot$ for reasonable values of $f \gtrsim 10^{-4}$. The thermal energy contained in the hot gas, $E_{th} \sim f^{1/2} 10^{54}$ ergs, is consistent with being generated by 1000 SNe each producing 10^{51} ergs in total energy if the conversion from kinetic to thermal energy is reasonably efficient.

The hot gas observed outside of the circumnuclear ring was likely produced within the ring and is escaping from pressure-confined clouds toward lower pressure regions perhaps in and likely above the plane of the galaxy.

Some of the gas escaping the circumnuclear ring undoubtedly makes its way into the sphere of influence of the nuclear supermassive black hole. We estimate there is ample fuel available at the center of the galaxy to power active galactic nucleus activity simply through Bondi accretion. However, the upper limit of $\sim 10^{37}$ ergs s^{-1} to the X-ray luminosity of any point source at

⁷ The CO measurements correspond to $n_H \sim 1.4 \times 10^{22}$ cm^{-2} , assuming a uniform distribution.

the nucleus suggests that the accretion is highly inefficient if the central object has a mass of $10^7 M_{\odot}$ as has been reported.

Evidence is ambiguous whether the outflowing hot gas is escaping as a galactic fountain or is confined by surrounding cold gas as a superbubble. No overlying layer of cold gas is evident in the X-ray spectrum; however, there is a dust lane to the southeast of the X-ray-emitting region that could confine the gas there as it appears to coincide with a decrease in the X-ray surface brightness. Perhaps the gas is rising away from the plane of the galaxy in a conical pattern: freely expanding vertically but constrained from moving laterally by ambient cold gas. If the flow at the edges of the cone is roughly tangential to the cold gas, then strong (shearing) shocks need not form and no limb-brightening need occur.

The estimated cooling timescale for this gas is as long as 350 Myr (scaling as $f^{1/2}$ and also dependent on the uncertain emission volume). Unless it is pressure confined, this gas could travel large distances before cooling and presumably falling back onto the galaxy in the form of molecular clouds. Although seen at a 40° inclination, there is no evidence that the gas has traveled more than about 500 pc from the ring. That is, fallback does not extend as far as the ends of the bar nor to the inner ring some 3 kpc away. What the source of material that produces the dust lanes visible along the leading edge of the bar is and how it is maintained or replenished is not revealed by the X-ray data.

The total estimated mass of hot gas in the ring and surrounding regions is $\sim 3 \times 10^6 M_{\odot}$. This is comparable to the estimated mass of warm, H α -emitting gas but only about 1% of the mass in molecular gas and 0.1% of the dynamical mass within the central ~ 1 kpc of NGC 3351. Thus, even if the hot gas escapes altogether it represents only a small fraction of the total mass budget: there is a substantial reservoir of potentially star-forming (cold) material available, enough to maintain star formation at a moderate rate for 100 Myr or longer within the inner regions of NGC 3351.

Support for this research was provided in part by NASA/*Chandra* Award Number GO5-6089A issued by the *Chandra* X-Ray Observatory Center, which is operated by the Smithsonian Astrophysical Observatory for and on behalf of NASA under contract NAS 8-03060. This work made use of observations made with the *Spitzer Space Telescope*, which is operated by the Jet Propulsion Laboratory, California Institute of Technology, under a contract with NASA and of related ground-based data obtained as part of the *Spitzer* Legacy Science project SINGS (Kennicutt et al. 2003), to which we are all greatly indebted. D. A. S. thanks A. Bykov for fruitful discussions and references on X-ray emission from star-forming clouds.

REFERENCES

- Anders, E., & Grevesse, N. 1989, *Geochim. Cosmochim. Acta*, 53, 197
 Ann, H. B., & Thakur, P. 2005, *ApJ*, 620, 197
 Bresolin, F., & Kennicutt, R. C. 2002, *ApJ*, 572, 838
 Buta, R. 1988, *ApJS*, 66, 233
 Buta, R., & Combes, F. 1996, *Fundam. Cosmic Phys.*, 17, 95
 Chevalier, R. A., & Clegg, A. W. 1985, *Nature*, 317, 44
 Chu, Y.-H., & Mac Low, M.-M. 1990, *ApJ*, 365, 510
 Colina, L., Garcia-Vargas, M. L., Mas-Hesse, J. M., Alberdi, A., & Krabbe, A. 1997, *ApJ*, 484, L41
 Contopoulos, G., & Papayannopoulos, T. 1980, *A&A*, 92, 33
 Devereux, N. A., Kenney, J. D. P., & Young, J. S. 1992, *AJ*, 103, 784
 Dong, X., & De Robertis, M. M. 2006, *AJ*, 131, 1236
 Elmegreen, B. G. 1994, *ApJ*, 425, L73
 ———. 2005, in *Island Universes: Structure and Evolution of Disk Galaxies* (Berlin: Springer), submitted (astro-ph/0510245)
 Elmegreen, D. M., Chromey, F. R., Santos, M., & Marshall, D. 1997, *AJ*, 114, 1850
 Ferrarese, L., & Merritt, D. 2000, *ApJ*, 539, L9
 Graham, A. W., Erwin, P., Caon, N., & Trujillo, I. 2003, *Rev. Mex. AA Ser. Conf.*, 17, 196
 Graham, J. A., et al. 1997, *ApJ*, 477, 535
 Grimm, H.-J., Gilfanov, M., & Sunyaev, R. 2003, *MNRAS*, 339, 793
 Immler, S., & Lewin, W. H. G. 2003, in *Supernovae and Gamma-Ray Bursters*, ed. K. Weiler (Berlin: Springer), 91
 Kennicutt, R., et al. 2003, *PASP*, 115, 928
 Leitherer, C., et al. 1999, *ApJS*, 123, 3
 Merloni, A., Heinz, S., & Di Matteo, T. 2003, *MNRAS*, 345, 1057
 Narayan, R. 2002, in *Lighthouses of the Universe: The Most Luminous Celestial Objects and Their Use for Cosmology*, ed. M. Gilfanov, R. Sunyaev, & E. Churazov (Berlin: Springer), 405
 Narayan, R., & Yi, I. 1994, *ApJ*, 428, L13
 Norman, C. A., Sellwood, J. A., & Hasan, H. 1996, *ApJ*, 462, 114
 Ott, J., Martin, C. L., & Walter, F. 2003, *ApJ*, 594, 776
 Planesas, P., Colina, L., & Perez-Olea, D. 1997, *A&A*, 325, 81
 Rubin, V. C., Ford, W. K., & Peterson, C. J. 1975, *ApJ*, 199, 39
 Sarzi, M., et al. 2002, *ApJ*, 567, 237
 Shull, J. M., & Saken, J. M. 1995, *ApJ*, 444, 663
 Sternberg, A., Hoffmann, T. L., & Pauldrach, A. W. A. 2003, *ApJ*, 599, 1333
 Strickland, D. K., Heckman, T. M., Colbert, E. J. M., Hoopes, C. G., & Weaver, K. A. 2004a, *ApJS*, 151, 193
 ———. 2004b, *ApJ*, 606, 829
 Strickland, D. K., Heckman, T. M., Weaver, K. A., Hoopes, C. G., & Dahlem, M. 2002, *ApJ*, 568, 689
 Suchkov, A. A., Berman, V. G., Heckman, T. M., & Balsara, D. S. 1996, *ApJ*, 463, 528
 Tyler, K., Wuillen, A. C., LaPage, A., & Rieke, G. H. 2004, *ApJ*, 610, 213
 Wang, Q. D. 2005, in *ASP Conf. Ser. 331, Extra-Planar Gas*, ed. R. Braun (San Francisco: ASP), 329
 Wang, Q. D., Immler, S., Walterbos, R., Lauroesch, J. T., & Breitschwerdt, D. 2001, *ApJ*, 555, L99
 Weaver, R., McCray, R., Castor, J., Shapiro, P., & Moore, R. 1977, *ApJ*, 218, 377
 Wyse, R. F. G. 2004, *ApJ*, 612, L17
 Wyse, R. F. G., Gilmore, G., & Franx, M. 1997, *ARA&A*, 35, 637